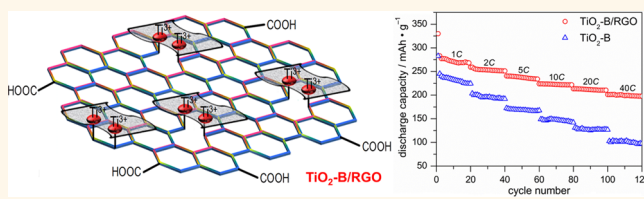


Chemically Bonded TiO_2 –Bronze Nanosheet/Reduced Graphene Oxide Hybrid for High-Power Lithium Ion Batteries

Vinodkumar Etacheri, Joseph E. Yourey, and Bart M. Bartlett*

Department of Chemistry, University of Michigan 930 North University Avenue, Ann Arbor, Michigan 48109-1055, United States

ABSTRACT Although Li-ion batteries have attracted significant interest due to their higher energy density, lack of high rate performance electrode materials and intrinsic safety issues challenge their commercial applications. Herein, we demonstrate a simple photocatalytic reduction method that simultaneously reduces graphene oxide (GO) and anchors (010)-faceted mesoporous bronze-phase titania (TiO_2 –B) nanosheets to reduced graphene oxide (RGO) through Ti^{3+} –C bonds. Formation of Ti^{3+} –C bonds during the photocatalytic reduction process was identified using electron paramagnetic resonance (EPR) and X-ray photoelectron spectroscopy (XPS) techniques. When cycled between 1–3 V (vs $\text{Li}^{+}/\text{Li}^{+}$), these chemically bonded TiO_2 –B/RGO hybrid nanostructures show significantly higher Li-ion storage capacities and rate capability compared to bare TiO_2 –B nanosheets and a physically mixed TiO_2 –B/RGO composite. In addition, 80% of the initial specific (gravimetric) capacity was retained even after 1000 charge–discharge cycles at a high rate of 40C. The improved electrochemical performance of TiO_2 –B/RGO nanoarchitectures is attributed to the presence of exposed (010) facets, mesoporosity, and efficient interfacial charge transfer between RGO monolayers and TiO_2 –B nanosheets.



KEYWORDS: lithium ion batteries · nanosheets · reduced graphene oxide · titanium dioxide · anode

Rechargeable Li-ion batteries are now common in the area of electrochemical energy storage due to their high energy density and wide range of applications in portable electronic devices, implantable medical devices, and electric vehicles.^{1–10} Despite these advantages, Li-ion batteries lack the high power density (rate performance) critical for many commercial applications.^{9,10} One of the main challenges is obtaining excellent rate capability while maintaining long cycle life and safety. The use of graphite anodes (theoretical capacity of 372 mAh/g) is one of the critical factors limiting the performance and safety of current generation Li-ion batteries. Consequently, numerous efforts have been devoted to developing safe, high-performance transition-metal oxide anode materials.^{11–13} Bronze-phase titania (TiO_2 –B) has attracted significant interest due to its excellent rate capability compared to other polymorphs of TiO_2 and titanates.^{14,15} In addition, TiO_2 –B has

high chemical stability and a smaller volume change (<3%) during lithium insertion/extraction.^{15–20} Moreover, the higher working voltage of TiO_2 –B (1.0–1.5 V vs $\text{Li}^{+}/\text{Li}^{+}$) eliminates the possibility of lithium plating that is commonly observed with graphite.

Despite the advantages, TiO_2 –B has poor electronic and ionic conductivity, which limits its application as a potential high-power anode material.^{15,21} Superior electronic and ionic conductivities of electrode materials are the key requirements for attaining high rate performance. Fabricating nanostructures is an established method for improving the electronic conductivity and Li^{+} diffusion kinetics in battery materials.^{20,22,23} Nanostructured electrodes facilitate better contact with the electrolyte solution and result in improved Li^{+} solubility, shorter length for Li^{+} and e^{-} transport, and superior interfacial kinetics. TiO_2 –B nanosheets exhibit superior electrochemical performance and faster interfacial charge-transfer kinetics

* Address correspondence to bartmb@umich.edu.

Received for review October 23, 2013 and accepted January 21, 2014.

Published online January 21, 2014
10.1021/nn405534r

© 2014 American Chemical Society

compared to nanotubes, nanowires, and nanoparticle morphologies.^{15,24} Moreover, porosity has a significant effect on the performance. For instance, significantly higher specific capacities and rate capability have been reported for mesoporous TiO_2 –B compared to nanoparticles.¹⁷ Since TiO_2 –B has open channels along the [010] axis, exposure of (010) facets could be beneficial for improving Li-transport.^{14,18}

Another widely used method to improve the rate capability of TiO_2 is anchoring it to electrically conducting substrates such as reduced graphene oxide (RGO).^{25–33} The greater electronic conductivity, high surface area, structural flexibility, and chemical stability of these carbonaceous substrates make them excellent supports for electrode materials. The advantage of anchoring TiO_2 nanoparticles to RGO sheets is that high surface area electrodes are maintained without the agglomeration of TiO_2 nanoparticles and/or restacking of RGO sheets.^{32–34} Therefore, we sought to combine the advantages of a nanosheet morphology, mesoporosity, exposure of (010) facets, and anchoring to carbonaceous substrates to attain high-performance TiO_2 –B anodes.

Many synthetic strategies have been reported for TiO_2 /RGO hybrid nanostructures.^{25–38} To the best of our knowledge, Ti–C bond formation, which is crucial for rapid interfacial charge transfer, has never been explicitly identified in TiO_2 /RGO hybrids. Herein we report a synthetic approach that involves simultaneous photocatalytic reduction of graphene oxide (GO) onto (010)-facet exposed mesoporous TiO_2 –B nanosheets using UV light, which results in reduced graphene oxide (RGO) anchored through Ti^{3+} –C bonds. By illuminating the ethanolic suspension of TiO_2 –B nanosheets and GO, photogenerated conduction-band electrons in TiO_2 reduce GO to RGO (with ethanol scavenging valence-band holes). In addition, surface Ti^{4+} ions of TiO_2 –B nanosheets get reduced to Ti^{3+} . Further reaction of Ti^{3+} surface states with defect carbon of the RGO gives rise to Ti^{3+} –C bonds (Figure 1).

RESULTS AND DISCUSSION

The X-ray diffraction pattern of GO has a distinctive (001) Bragg reflection at $9.8^\circ 2\theta$, which corresponds to the interlayer spacing of 9.0 \AA between the individual GO sheets (Figure 2a).^{39,40} The diffraction peak characteristic of graphite flakes ($26.6^\circ 2\theta$) is absent in these samples, supporting the complete oxidation of graphite to GO. The well-resolved XRD pattern of the TiO_2 –B nanosheets (Figure 2a) is in good agreement with previous reports (ICDD 046–1237).^{22,41,42} Unlike other synthesis methods, anatase impurities are not detected in our TiO_2 –B nanosheet samples. There are no characteristic XRD peaks of GO and RGO observed in TiO_2 –B/RGO nanostructures (Figure 2a). This result is attributed to the destruction of the regular stacking of GO upon anchoring the TiO_2 –B nanosheets. The phase purity of TiO_2 –B nanosheets, GO, and RGO was further confirmed using

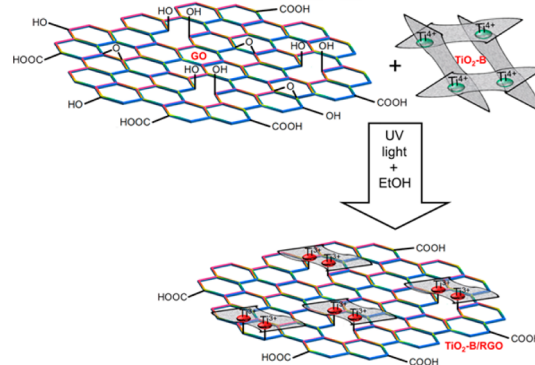


Figure 1. Synthesis of the TiO_2 –B/RGO hybrid nanostructure through photocatalytic reduction.

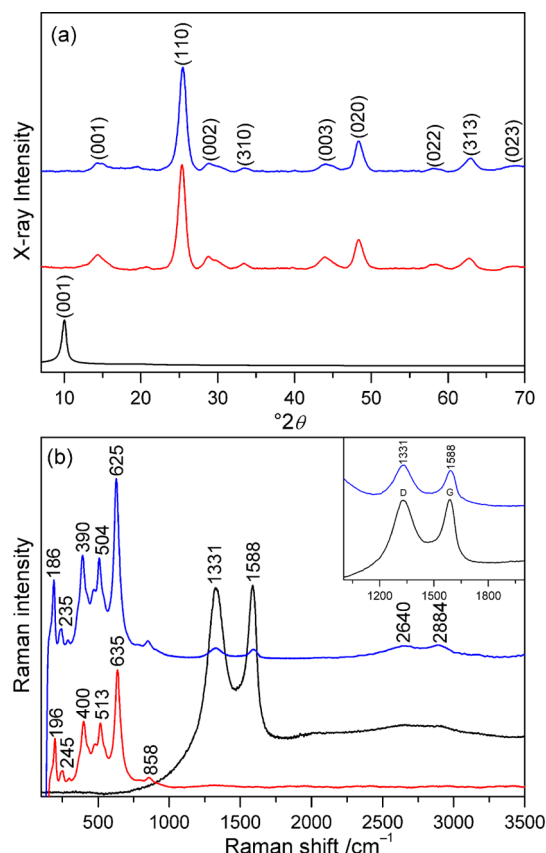


Figure 2. (a) X-ray diffraction patterns of GO (black), TiO_2 –B (red), and TiO_2 –B/RGO hybrid (blue). (b) Raman spectra of GO (black), TiO_2 –B (red), and TiO_2 –B/RGO hybrid (blue). Inset: D and G bands of GO and RGO.

Raman spectroscopy (Figure 2b). In the case of titania, Raman modes at $196, 245, 400, 513, 635$, and 858 cm^{-1} are characteristic of phase-pure TiO_2 –B.^{15,17,43}

The 2-D nanosheet morphology of TiO_2 –B is evident from the absence of $\text{Ti}–\text{O}–\text{Ti}$ and $\text{O}–\text{Ti}–\text{O}$ torsional modes at 140 and 150 cm^{-1} .^{15,17} As prepared, GO exhibits two distinct Raman peaks. The D-band at 1331 cm^{-1} is characteristic of disordered sp^2 carbon.^{39,44,45} The other band at 1588 cm^{-1} corresponds to graphitized structures, which is known as the G-band.⁴⁶ After photocatalytic reduction, the positions of these Raman bands are

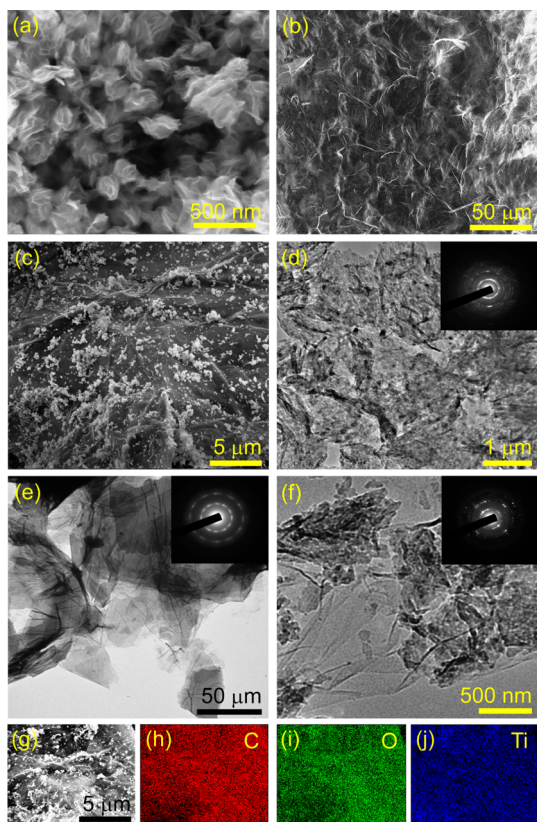


Figure 3. SEM images of (a) TiO_2 –B, (b) GO, (c) TiO_2 –B/RGO hybrid. TEM images and SAED patterns of (d) TiO_2 –B, (e) GO, (f) TiO_2 –B/RGO hybrid. (g) SEM image and corresponding EDX maps of (h) carbon, (i) oxygen and (j) titanium in the TiO_2 –B/RGO hybrid.

unchanged, although an increased D/G intensity ratio is identified for the TiO_2 –B/RGO nanostructure compared to that of pure GO. This observation reveals a decrease in the average size of the in-plane sp^2 domains and oxidized molecular defects, which confirm the photocatalytic reduction of GO.^{39,47} The bathochromic shift in the TiO_2 –B Raman bands for TiO_2 –B/RGO hybrid suggests a strong interaction between RGO and the individual TiO_2 –B nanosheets. Moreover, the 2D band of TiO_2 –B/RGO at 2640 cm^{-1} implies that RGO exists as single layers in the hybrid.⁴⁸

SEM images demonstrate the formation of highly agglomerated TiO_2 –B nanosheets with an average thickness of $\sim 10\text{ nm}$ (Figure 3a). As prepared, $\sim 30\text{ }\mu\text{m}$ sized GO sheets are also highly agglomerated, which is characteristic of high surface area materials (Figure 3b). It is clear that photocatalytic reduction results in the uniform anchoring of TiO_2 –B nanosheets on micrometer-sized RGO sheets. In this case, parts of the RGO sheets are still exposed (Figure 3c), which is critical for maintaining good contact between individual RGO sheets for high electronic conductivity. The compositional purity of the TiO_2 –B nanosheets, GO, and TiO_2 –B/RGO hybrid nanostructures was also demonstrated by their EDX patterns (Figures S1 and S2, Supporting Information). As evidenced from the TEM images, individual TiO_2 –B

nanosheets are $\sim 100 \times 120\text{ nm}$ sized and were highly agglomerated (Figure 3d). Individual $\sim 30 \times 50\text{ }\mu\text{m}$ sized GO sheets restack into multiple layers (Figure 3e), which agrees well with the interlayer spacing of 9.0 \AA observed from the XRD pattern. No such restacking occurs in the case of the TiO_2 –B/RGO hybrid (Figure 3f and Figure S3, Supporting Information). This result can be attributed to the anchoring of TiO_2 –B nanosheets onto individual RGO sheets during the photocatalytic reduction, which prevents restacking.

As prepared, GO shows a distinct selected area electron diffraction (SAED) pattern, suggestive of an ordered carbon framework. The SAED pattern of TiO_2 –B nanosheets contains a series of well-defined Debye–Scherrer rings confirming their polycrystalline nature. The calculated *d*-spacing values of $3.0, 3.5, 3.7, 6.2$, and 7.1 \AA correspond to Miller indices (002), (400), (110), (001), and (200) of TiO_2 –B. Diffraction patterns of both TiO_2 –B and RGO are present in the SAED pattern of the hybrid nanostructures, which verifies their nanoscale mixing. Lattice fringes spaced at 3.0 and 3.5 \AA in the high-resolution transmission electron microscopy (HRTEM) images (Figure S4, Supporting Information) correspond to (400) and (002) Miller indices. The 107° angle between these facets is characteristic of monoclinic TiO_2 –B, and therefore, the exposed facets of these nanosheets can be indexed as the (010) planes.^{14,49}

To gain further insight into the structure of TiO_2 –B/RGO hybrid nanostructures, we performed EDX elemental mapping. As presented in Figure 3g–j, titanium, oxygen, and carbon atoms are homogeneously distributed in TiO_2 –B/RGO hybrid nanostructures. Atomic force microscopy (AFM) measurements on GO demonstrate an average thickness of 70 nm , which corresponds to ~ 60 layers of restacked sheets (Figure S5, Supporting Information). Nitrogen adsorption–desorption isotherms of the TiO_2 –B/RGO hybrids show type-IV characteristics with H3-type hysteresis (Figure S6, Supporting Information) associated with the presence of slit like pores.³⁹ The Brunauer–Emmett–Teller (BET) analysis gives a specific surface area of $160\text{ m}^2/\text{g}$. The pore volume ($0.21\text{ cm}^3/\text{g}$) and pore diameter (9.5 nm) were determined from Barret–Joyner–Halenda (BJH) analysis. These results highlight that the (010) facet-exposed mesoporous TiO_2 –B nanosheets are homogeneously anchored on RGO monolayers.

Electron paramagnetic resonance (EPR) spectroscopy tells the chemical state of titanium (Figure 4). The TiO_2 –GO sample has no characteristic EPR resonances at 77 K , whereas the TiO_2 –B/RGO hybrid nanostructure shows an EPR resonance at $g = 1.94$, indicative of surface Ti^{3+} .⁵⁰ Comparing the signal intensity of the TiO_2 –B/RGO hybrids to those of standard Ti^{4+} solutions reveal that one in $6.1 \times 10^5\text{ Ti}^{4+}$ ions is reduced to Ti^{3+} during the photocatalytic reduction, which is comparable to the Ti^{3+} content present in chemically reduced TiO_2 .⁵¹ We note that Ti^{3+} ions formed during the photocatalytic

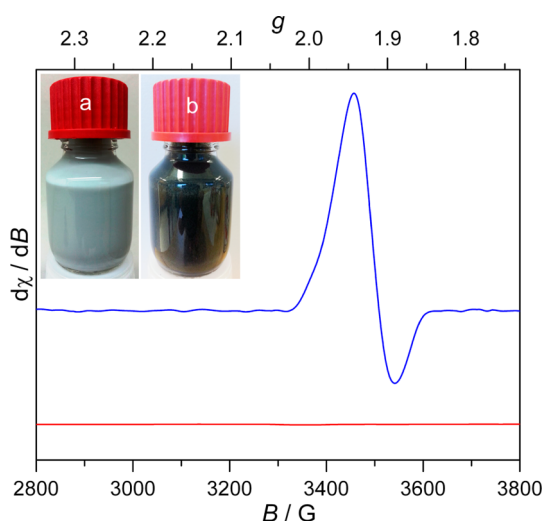


Figure 4. EPR spectra of $\text{TiO}_2\text{--B}$ (red) and $\text{TiO}_2\text{--B/RGO}$ hybrid (blue). Inset: photographs of $\text{TiO}_2\text{--B/GO}$ in absolute ethanol (a) before and (b) after photoreduction.

reduction are stable upon exposure to air. To probe the reaction mechanism, EPR spectra were collected for the ethanolic suspension of pure $\text{TiO}_2\text{--B}$ nanosheets before and after the UV-light treatment (Figure S7, Supporting Information). After UV treatment, the EPR spectrum of the $\text{TiO}_2\text{--B}$ nanosheets presents a band at $g = 1.94$, and the solution shows a corresponding blue color, all characteristic of surface Ti^{3+} .

The simultaneous photocatalytic reduction of GO and anchoring of $\text{TiO}_2\text{--B}$ nanosheets on the RGO sheets was further characterized by XP spectroscopy. Three typical peaks are observed in GO, which represent chemically different species are located at 284.5, 286.8, and 288.5 eV, respectively (Figure 5a). These peaks correspond to elemental carbon/ sp^2 -hybridized carbon from GO, oxygen-containing alcohol, or ether linkages (C--OH and C--O) and carboxylate (O=C--O), respectively.^{39,44,52} In the case of $\text{TiO}_2\text{--B/RGO}$ hybrid nanostructures, the high intensity peak at 286.8 eV disappears, and an additional peak characteristic of defect-containing sp^2 -hybridized carbon emerges at 286.0 eV (Figure 5b). This shift indicates that most of the oxygen-containing functional groups of GO are efficiently reduced during the photocatalytic reduction reaction. A low intensity peak of carboxyl carbon (288.5 eV) is still present in the photoreduced sample. An additional C(1s) peak at 283.5 eV emerges, which is at higher binding energy than the titanium carbide ($\text{Ti}^{4+}\text{--C}$) peak at 281.5 eV. It can be assigned to carbon from RGO bonded to Ti^{3+} of $\text{TiO}_2\text{--B}$ nanosheets.^{53,54} $\text{Ti}^{3+}\text{--C}$ bond formation is corroborated by the bathochromic shift observed for the Raman spectrum of $\text{TiO}_2\text{--B/RGO}$ compared to that of bare $\text{TiO}_2\text{--B}$ nanosheets.

The appearance of $\text{Ti}(2\text{p})$ peaks of $\text{TiO}_2\text{--B/RGO}$ hybrids at higher binding energies (Figure S8) compared to pure $\text{TiO}_2\text{--B}$ can be attributed to the electron-withdrawing inductive effect of the residual carboxylate

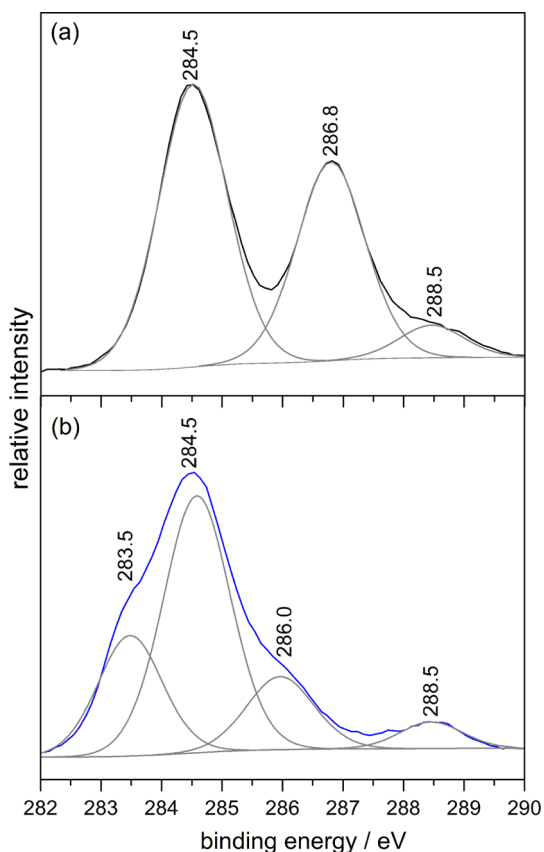


Figure 5. C(1s) XP spectra of (a) GO and (b) $\text{TiO}_2\text{--B/RGO}$ hybrid.

on RGO.^{55,56} The photocatalytic reduction of GO is also evidenced by the color change from gray to black (Figure 4 inset), which has previously been observed during the chemical reduction of GO and assigned to the partial restoration of the π conjugated network of graphene.⁵⁷

The as-prepared GO displays characteristic IR absorption bands of several oxygen-containing groups (Figure 6). The prominent bands at 1732 and 3407 cm^{-1} can be ascribed to C=O stretching and O--H stretching, respectively. Then, small peaks at 1059 and 1224 cm^{-1} correspond to C--O (alkoxy) and C--O (epoxy) stretches, respectively.^{47,56} The C=C skeleton vibration appears at 1620 cm^{-1} .⁵⁸ The absorption bands of most oxygen-containing functional groups are absent in the $\text{TiO}_2\text{--B/RGO}$ hybrid nanostructures obtained after photocatalytic reduction. The low intensity band observed at 789 cm^{-1} corresponds to carboxyl groups that persist in the photoreduced sample. These observations imply that carbon–oxygen single bonds are completely reduced during the photocatalytic reduction, and carboxyl groups remain unaffected, which is in good agreement with the XPS results. Additionally, the broad IR band centered at 558 cm^{-1} for pure $\text{TiO}_2\text{--B}$ and $\text{TiO}_2\text{--B/RGO}$ hybrid represents the Ti--O stretching mode in crystalline TiO_2 .^{59,60} The fact that this band is isoenergetic for

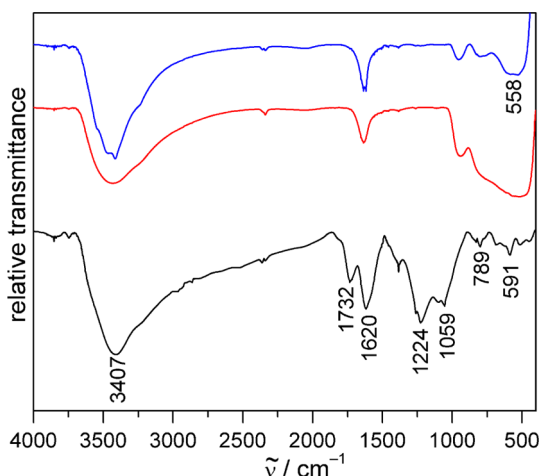


Figure 6. FTIR spectra of GO (black), TiO_2 –B (red), and TiO_2 –B/RGO hybrid (blue).

both TiO_2 –B and TiO_2 –B/RGO confirms that our photocatalytic reduction results in forming Ti^{3+} only at the surface, and not within the bulk. Thus, XPS, EPR, and FTIR measurements clearly demonstrate the efficient photocatalytic reduction of GO and anchoring of TiO_2 –B nanosheets on RGO through Ti^{3+} –C bonds. Although the photocatalytic anchoring of TiO_2 onto RGO has been previously reported, the formation Ti–C bonds has not been observed or proposed.^{32,35} The mechanism of the photocatalytic GO reduction can be explained by the photogeneration of electron–hole pairs on TiO_2 –B surface. Upon UV irradiation, electrons are excited to the conduction band (CB) leaving a hole in the valence band (VB) of TiO_2 –B. Consumption of holes by ethanol results in the accumulation of photo-excited electrons, which simultaneously reduce GO and Ti^{4+} ions. Subsequent reactions between Ti^{3+} surface states and defect carbon moieties of RGO result in Ti^{3+} –C bond formation. This method is environmentally benign. It does not require toxic reducing agents such as hydrazine. Moreover, the degree of reduction can be tuned by varying the irradiation time, and simply evaporating the solvent can isolate the product.

We then evaluated the electrochemical performance of the TiO_2 –B nanosheets and TiO_2 –B/RGO hybrid by galvanostatic discharge–charge measurements at different rates. The voltage profile of the TiO_2 –B/RGO hybrid electrode at varying current densities is presented in Figure 7a. A slope throughout the voltage profile is identical to that of TiO_2 –B nanostructures reported previously.^{15,16} At a discharge rate of 1C (the current required to discharge the theoretical capacity in 1 h, 335 mA/g), TiO_2 –B nanosheets exhibit a gravimetric capacity of 225 mAh/g, which is comparable to that of nanoparticles, and nanotubes.^{16,61} In contrast, TiO_2 –B/RGO hybrid electrodes achieved a higher specific capacity of 275 mAh/g at the same 1C current. Upon increasing the load, TiO_2 –B nanosheets experience severe capacity loss, whereas TiO_2 –B/RGO

hybrid electrodes show only minor capacity fading and exhibit a high specific capacity of 200 mAh/g even at 40C current. This capacity is 2.5-fold higher than that of TiO_2 –B nanosheets and that of a physical mixture of TiO_2 –B with RGO (Figure 7b). Also notable is that the Coulombic efficiency of these hybrid electrodes reaches nearly 100% after four charge–discharge cycles at 1C current, and retain a high efficiency of 99% at 40 C current (Figure S9, Supporting Information). The electrochemical stability of TiO_2 –B/RGO nanostructured electrodes is determined by long-term galvanostatic cycling at various charge–discharge rates. Independent of the current densities, these electrodes maintain 80% of the initial capacity even after 1000 cycles (Figure 7c). In contrast, a physical mixture of TiO_2 –B and RGO retains only 20% of the initial capacity under the same experimental conditions (Figure S10, Supporting Information). To the best of our knowledge, this high specific capacity, rate performance, and capacity retention is superior to any of the reported TiO_2 –B anodes for Li-ion batteries. Although the specific capacity of TiO_2 –B/RGO hybrid is not greater than that observed in other anode materials, we observe excellent capacity at high current.

In order to get further insight into the rate capability, electrochemical impedance spectroscopy (EIS) was performed on electrodes composed of TiO_2 –B, chemically bonded TiO_2 –B/RGO hybrids and a physical mixture of TiO_2 –B and RGO. As shown in Figure 7d, the Nyquist plots for all three samples display a single semicircle in the high frequency region and a sloping straight line in the low frequency range, corresponding to charge-transfer resistance (R_{ct}) and solid-state diffusion of lithium in this insertion material (Z_w) respectively.^{32,62} The smaller semicircle diameter for TiO_2 –B/RGO electrode clearly demonstrates a smaller R_{ct} for chemically bonded TiO_2 –B/RGO compared to the physical mixture and conventional TiO_2 –B/carbon black composite electrodes. The significantly better electrochemical performance of the TiO_2 –B/RGO hybrid can be explained by the unique nanoarchitecture with the promising features of mesoporosity and exposed (010) facets.

The high surface area of 2D ultrathin TiO_2 –B nanosheets facilitates a large electrolyte-electrode contact area and shorter diffusion length for Li^+ , and it better accommodates large strain due to volume changes upon lithium insertion and extraction, all of which are favorable for achieving high rate capability. Moreover, anchoring TiO_2 –B nanosheets onto RGO through Ti^{3+} –C bonds effectively enhances the electronic conductivity (interfacial charge transfer) leading to rapid electrochemical reactions. In addition, anchoring the TiO_2 –B nanosheets onto RGO sheets minimizes TiO_2 agglomeration and RGO sheet restacking, which helps to maintain high surface areas and stability during lithium insertion/extraction.

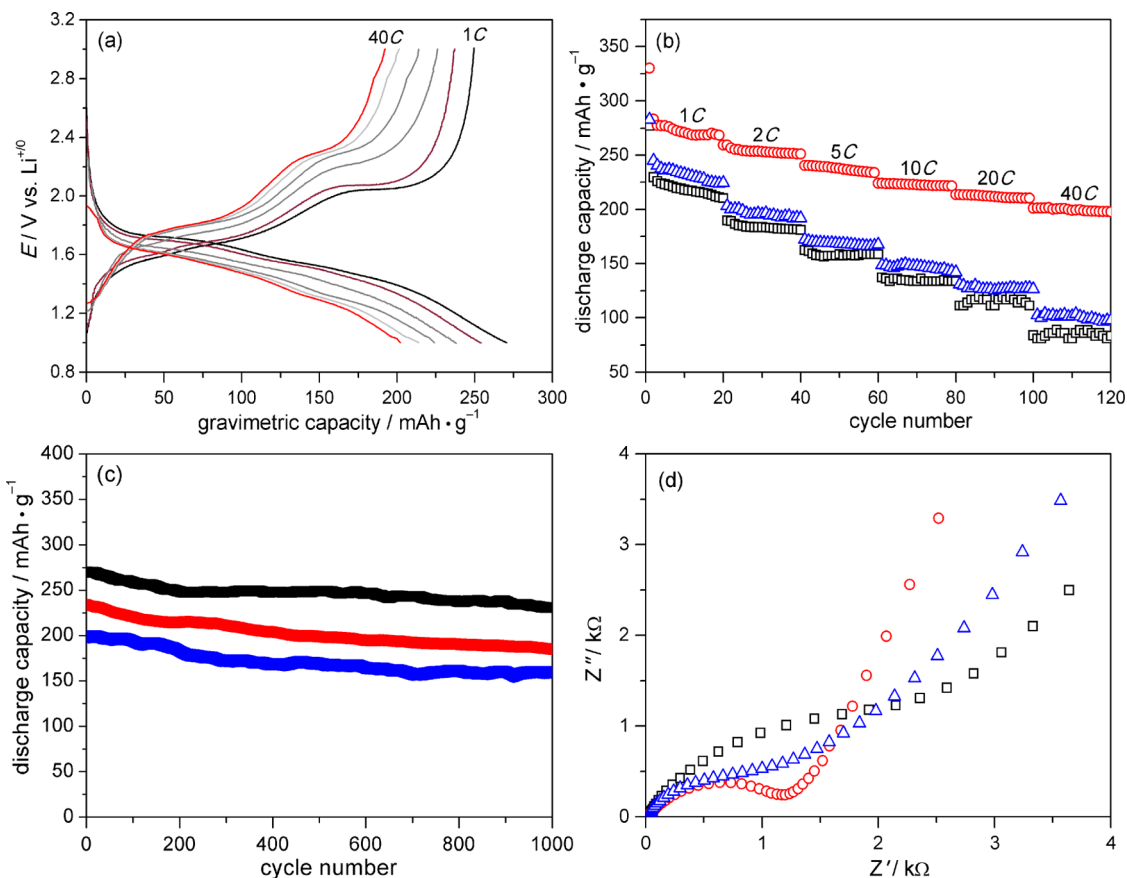


Figure 7. (a) Second discharge-charge profiles of TiO₂-B/RGO hybrid electrodes at various rates; (b) discharge capacity of TiO₂-B/RGO hybrid (red) TiO₂-B + RGO (blue) and TiO₂-B (black) at varying rate; (c) long-term galvanostatic cycling of TiO₂-B/RGO hybrid electrodes at 1C (black) 20C (red) and 40C (blue) current; (d) Nyquist plots of TiO₂-B/RGO hybrid (red) TiO₂-B + RGO mixture (blue) and TiO₂-B (black).

CONCLUSIONS

We have chemically bonded (010)-faceted mesoporous TiO₂-B nanosheets to RGO sheets through a photocatalytic reduction method resulting in the formation of Ti³⁺-C bonds. These TiO₂-B/RGO hybrid nanostructures demonstrate superior specific capacity, excellent rate capability, and capacity retention compared to a physical mixture of TiO₂-B and RGO and a conventional TiO₂-B/carbon black composite electrode. We attribute the higher electrochemical performance of TiO₂-B/RGO hybrid

nanostructures to efficient interfacial charge transfer between TiO₂-B nanosheets and RGO, which is fostered by Ti³⁺-C bonds. Our work demonstrates that the bonding interaction between conducting carbon and the active electrode material is a crucial factor for determining the electrochemical performance of Li-ion batteries. The chemically bonded TiO₂-B/RGO hybrid nanostructure that operates in the safe voltage range (1–3 V vs Li⁺/0) is a potential candidate for replacing graphite anodes in conventional Li-ion batteries.

EXPERIMENTAL SECTION

Material Synthesis. All reagents were purchased from Sigma-Aldrich and used without further purification. Ultrathin TiO₂-B nanosheets were synthesized by a hydrothermal method reported by Xiang *et al.*¹⁴ In a typical synthetic procedure, 4 mL of TiCl₃ (20% aqueous solution in HCl) and 4 mL of deionized water were mixed with 50 mL of ethylene glycol. After being stirred for 10 min, the mixture was heated to 150 °C for 6 h in four sealed 23 mL Teflon-lined autoclaves (Parr instruments); heating and cooling rates were 10 °C/min. After cooling, the products were separated by centrifugation and washed with water and

ethanol four times. Powder samples were dried at 60 °C in a vacuum oven and annealed at 400 °C for 2 h. Graphene oxide nanosheets were synthesized from graphite flakes by an improved Hummers' method.⁴⁰ Briefly, 9:1 mixture of concentrated H₂SO₄/H₃PO₄ (120:13.3 mL) was added to a mixture of graphite flakes (1.0 g) and KMnO₄ (6.0 g). The reaction was then heated to 50 °C, stirred for 12 h, cooled to room temperature, and poured onto ice (200 mL) with 30% H₂O₂ (2 mL). The mixture obtained was centrifuged (4000 rpm for 4 h), and the supernatant was decanted. The remaining solid material was then washed in succession with 200 mL of water, 200 mL of 30% HCl, and 200 mL of ethanol. The material obtained after an

extended, multiple-washing process was dried overnight in a vacuum oven at 60 °C. TiO_2 –B nanosheets were chemically bonded to RGO through a photocatalytic–reduction method. In a typical synthesis, a homogeneous GO suspension was first obtained by sonicating GO (20 mg) in absolute ethanol (100 mL) for 30 min. The suspension obtained was then mixed with TiO_2 –B nanosheets (70 mg) and irradiated with UV light (150 W) for 12 h under constant stirring to form the chemically bonded TiO_2 –B/RGO hybrid. The sample was then centrifuged and washed with deionized water three times and dried in a vacuum oven at 60 °C. For comparing the electrochemical performance, separately prepared RGO was physically mixed with TiO_2 –B nanosheets.

Characterization. A Bruker D8 advance diffractometer equipped with a Lynx-Eye detector and parallel beam optics using $\text{Cu K}\alpha$ radiation ($\lambda = 0.154184$ nm) was employed for collecting the X-ray diffraction (XRD) patterns of the samples ($2\theta = 10$ –70°). The room-temperature Raman analysis of samples was performed using a Renishaw inVia Reflex micro-Raman system equipped with a 633 nm Ar^+ ion laser. The microstructure and morphology of samples were systematically investigated using HR-SEM (Inspect FEI Nova-200), UHR-TEM (JEOL JEM-3011), and AFM (Veeco Dimension Icon). Nitrogen adsorption–desorption isotherms were collected using a Quantachrome Nova 4200e surface area analyzer. X-band electron paramagnetic resonance (EPR) spectra of the samples were collected at liquid nitrogen temperature using a Bruker EMX spectrometer. Ti^{3+} formed during the photocatalytic reduction was quantified by comparing the EPR spectral intensity of the TiO_2 –B/RGO hybrid to a calibration curve constructed from standard Ti^{3+} solutions (1–10 mM TiCl_3) in ethanol at 77 K. X-ray photoelectron spectra (XPS) were recorded using a Kratos Axis Ultra spectrometer equipped with an $\text{Al K}\alpha$ X-ray radiation source (photon energy 1486.6 eV). The binding energies of all elements present were determined by setting the CC/CH component of the C 1s peak at 284.5 eV. After removing a nonlinear Shirley background, high-resolution, core-level spectra were used for quantitative surface chemical analysis. Vision software (Kratos) was used for deconvoluting the XPS spectra into Gaussian/Lorenzian-shaped components. A Perkin-Elmer GX spectrometer was used for recording the FTIR spectra of samples (in the range of 4000–400 cm^{-1}).

Electrochemistry. Electrochemical experiments were carried out at room temperature in Swagelok-type cells using a Celgard 3401 polypropylene separator and Li-foil as both the auxiliary and pseudoreference electrode. The electrolyte was purchased from MTI Corporation, which consists of 1 M LiPF_6 in a 1:1:1 mixture of ethylene carbonate (EC)/dimethyl carbonate (DMC)/diethyl carbonate (DEC). The working electrode consists of 90 wt % of the active material (70% TiO_2 –B + 20% RGO obtained after photoreduction) and 10 wt % of binder (styrene butadiene rubber/sodium carboxymethyl cellulose 1:1 by weight). A control electrode was also prepared by mixing 70 wt % of TiO_2 –B with 20 wt % carbon black and 10 wt % binder. The active material loading of the working electrodes was 1–2 mg/cm². The electrochemical cells were assembled in high-purity argon (99.9995%) filled glovebox (Vacuum Atmospheres) equipped with O_2 and H_2O absorbers. Galvanostatic charge–discharge cycling of these two electrode cells in the potential range of 1.0–3.0 V (vs. Li^{+}/Li) was performed using a custom-built Vencon UBA5 battery analyzer. The electrode capacity calculations were made in triplicate, and the results were within the 5% error limit. A potentiostat (Autolab PGSTAT302) coupled with a frequency response analyzer (Solartron 1255) was used for the electrochemical impedance spectroscopy (EIS) measurements.

Conflict of Interest: The authors declare no competing financial interest.

Acknowledgment. We thank the University of Michigan Energy Institute for a Postdoctoral Partnerships for Innovation Fellowship for V.E. This work was supported by funding from the National Science Foundation (DMR-1253347). Spectroscopic (XPS) and microscopic (SEM, TEM, and AFM) characterization techniques at the University of Michigan Electron Microbeam

Analysis Laboratory were funded by NSF Grant Nos. DMR-0320710 and DMR-0315633, respectively.

Supporting Information Available: EDX pattern of TiO_2 –B nanosheets and GO, EDX pattern of TiO_2 –B/RGO, TEM image of TiO_2 –B/RGO, HRTEM image of TiO_2 –B nanosheets, AFM image of GO, N_2 adsorption–desorption results of TiO_2 –B nanosheets, EPR spectra of TiO_2 –B nanosheets before and after UV-light irradiation, Ti (2p) XPS pattern of TiO_2 –B and TiO_2 –B/RGO, Coulombic efficiency of TiO_2 –B/RGO at various current densities, and long-term galvanostatic cycling performance of a physically mixed TiO_2 –B and RGO sample. This material is available free of charge via the Internet at <http://pubs.acs.org>.

REFERENCES AND NOTES

- Kang, B.; Ceder, G. Battery Materials for Ultrafast Charging and Discharging. *Nature* **2009**, *458*, 190–193.
- Goodenough, J. B.; Kim, Y. Challenges for Rechargeable Li Batteries. *Chem. Mater.* **2010**, *22*, 587–603.
- Etacheri, V.; Marom, R.; Elazari, R.; Salitra, G.; Aurbach, D. Challenges in the Development of Advanced Li-Ion Batteries: a Review. *Energy Environ. Sci.* **2011**, *4*, 3243–3262.
- Liddle, B. J.; Collins, S. M.; Bartlett, B. M. New One-Pot Hydrothermal Synthesis and Electrochemical Characterization of $\text{Li}_{1+x}\text{Mn}_{2-y}\text{O}_4$ Spinel Structured Compounds. *Energy Environ. Sci.* **2010**, *3*, 1339–1346.
- Armand, M.; Gruegeon, S.; Vezin, H.; Laruelle, S.; Ribiere, P.; Poizot, P.; Tarascon, J. M. Conjugated Dicarboxylate Anodes for Li-Ion Batteries. *Nat. Mater.* **2009**, *8*, 120–125.
- Etacheri, V.; Geiger, U.; Gofer, Y.; Roberts, G. A.; Stefan, I. C.; Fasching, R.; Aurbach, D. Exceptional Electrochemical Performance of Si-Nanowires in 1,3-Dioxolane Solutions: A Surface Chemical Investigation. *Langmuir* **2012**, *28*, 6175–6184.
- Etacheri, V.; Haik, O.; Gofer, Y.; Roberts, G. A.; Stefan, I. C.; Fasching, R.; Aurbach, D. Effect of Fluoroethylene Carboxylate (FEC) on the Performance and Surface Chemistry of Si-Nanowire Li-ion Battery Anodes. *Langmuir* **2012**, *28*, 965–976.
- Etacheri, V.; Sharon, D.; Garsuch, A.; Afri, M.; Frimer, A. A.; Aurbach, D. Hierarchical activated carbon microfiber (ACM) electrodes for rechargeable $\text{Li}–\text{O}_2$ batteries. *J. Mater. Chem. A* **2013**, *1*, 5021–5030.
- Hao, X.; Bartlett, B. M. $\text{Li}_4\text{Ti}_5\text{O}_{12}$ Nanocrystals Synthesized by Carbon Templating from Solution Precursors Yield High Performance Thin Film Li-Ion Battery Electrodes. *Adv. Energy Mater.* **2013**, *3*, 753–761.
- Yang, S.; Gong, Y.; Liu, Z.; Zhan, L.; Hashim, D. P.; Ma, L.; Vajtai, R.; Ajayan, P. M. Bottom-up Approach toward Single-Crystalline VO_2 -Graphene Ribbons as Cathodes for Ultrafast Lithium Storage. *Nano Lett.* **2013**, *13*, 1596–1601.
- Wang, J.; Yang, N.; Tang, H.; Dong, Z.; Jin, Q.; Yang, M.; Kisailus, D.; Zhao, H.; Tang, Z.; Wang, D. Accurate Control of Multishelled Co_3O_4 Hollow Microspheres as High-Performance Anode Materials in Lithium-Ion Batteries. *Angew. Chem., Int. Ed.* **2013**, *52*, 6417–6420.
- Poizot, P.; Laruelle, S.; Gruegeon, S.; Dupont, L.; Tarascon, J. M. Nano-Sized Transition-Metal Oxides as Negative-Electrode Materials for Lithium-Ion Batteries. *Nature* **2000**, *407*, 496–499.
- Idota, Y.; Kubota, T.; Matsufuji, A.; Maekawa, Y.; Miyasaka, T. Tin-Based Amorphous Oxide: A High-Capacity Lithium-Ion-Storage Material. *Science* **1997**, *276*, 1395–1397.
- Xiang, G.; Li, T.; Zhuang, J.; Wang, X. Large-Scale Synthesis of Metastable TiO_2 (B) Nanosheets with Atomic Thickness and Their Photocatalytic Properties. *Chem. Commun.* **2010**, *46*, 6801–6803.
- Etacheri, V.; Kuo, Y.; Ven, A. V.; Bartlett, B. M. Mesoporous TiO_2 –B Microflowers Composed of (110) Facet-Exposed Nanosheets for Fast Reversible Lithium-Ion Storage. *J. Mater. Chem. A* **2013**, *1*, 12028–12032.

16. Armstrong, A. R.; Armstrong, G.; Canales, J.; Bruce, P. G. $\text{TiO}_2\text{-B}$ Nanowires. *Angew. Chem. Int. Ed.* **2004**, *43*, 2286–2288.

17. Dylla, A. G.; Lee, J. A.; Stevenson, K. J. Influence of Mesoporosity on Lithium-Ion Storage Capacity and Rate Performance of Nanostructured $\text{TiO}_2\text{(B)}$. *Langmuir* **2012**, *28*, 2897–2903.

18. Zukalová, M.; Kalbáč, M.; Kavan, L.; Exnar, I.; Graetzel, M. Pseudocapacitive Lithium Storage in $\text{TiO}_2\text{(B)}$. *Chem. Mater.* **2005**, *17*, 1248–1255.

19. Tsai, M. C.; Chang, J. C.; Sheu, H. S.; Chiu, H. T.; Lee, C. Y. Lithium Ion Intercalation Performance of Porous Laminal Titanium Dioxides Synthesized by Sol–Gel Process. *Chem. Mater.* **2009**, *21*, 499–505.

20. Ren, Y.; Liu, Z.; Pourpoint, F.; Armstrong, A. R.; Grey, C. P.; Bruce, P. G. Nanoparticulate $\text{TiO}_2\text{(B)}$: An Anode for Lithium-Ion Batteries. *Angew. Chem., Int. Ed.* **2012**, *51*, 2164–2167.

21. Dylla, A. G.; Henkelman, G.; Stevenson, K. J. Lithium Insertion in Nanostructured $\text{TiO}_2\text{(B)}$ Architectures. *Acc. Chem. Res.* **2013**, *46*, 1104–1112.

22. Armstrong, G.; Armstrong, A. R.; Canales, J.; Bruce, P. G. Nanotubes with the $\text{TiO}_2\text{-B}$ Structure. *Chem. Commun.* **2005**, 2454–2456.

23. Shin, K.; Kim, H. J.; Choi, J. M.; Choi, Y. M.; Song, M. S.; Park, J. H. Controlled Synthesis of Skein Shaped $\text{TiO}_2\text{-B}$ Nanotube Cluster Particles with Outstanding Rate Capability. *Chem. Commun.* **2013**, *21*, 2326–2328.

24. Liu, S.; Jia, H.; Han, L.; Wang, J.; Gao, P.; Xu, D.; Yang, J.; Che, S. Nanosheet-Constructed Porous $\text{TiO}_2\text{-B}$ for Advanced Lithium Ion Batteries. *Adv. Mater.* **2012**, *24*, 3201–3204.

25. Xin, X.; Zhou, X.; Wu, J.; Yao, X.; Liu, Z. Scalable Synthesis of TiO_2 /Graphene Nanostructured Composite with High-Rate Performance for Lithium Ion Batteries. *ACS Nano* **2012**, *6*, 11035–11043.

26. Ding, S.; Chen, J. S.; Luan, D.; Boey, F. Y. C.; Madhavi, S.; Wen, X. Graphene-Supported Anatase TiO_2 Nanosheets for Fast Lithium Storage. *Chem. Commun.* **2011**, *47*, 5780–5782.

27. He, L.; Ma, R.; Du, N.; Ren, J.; Wong, T.; Lia, Y.; Lee, S. T. Growth of TiO_2 Nanorod Arrays on Reduced Graphene Oxide with Enhanced Lithium-Ion Storage. *J. Mater. Chem.* **2012**, *22*, 19061–19066.

28. Ren, Y.; Zhang, J.; Liu, Y.; Li, H.; Wei, H.; Li, B.; Wang, X. Synthesis and Superior Anode Performances of TiO_2 –Carbon–rGO Composites in Lithium-Ion Batteries. *ACS Appl. Mater. Interfaces* **2012**, *4*, 4776–4780.

29. Cao, H.; Li, B.; Zhang, J.; Lian, F.; Kong, X.; Qu, M. Synthesis and Superior Anode Performance of TiO_2 @Reduced Graphene Oxide Nanocomposites for Lithium Ion Batteries. *J. Mater. Chem.* **2012**, *22*, 9759–9766.

30. Li, W.; Wang, F.; Feng, S.; Wang, J.; Sun, Z.; Li, B.; Li, Y.; Yang, J.; Elzatahry, A. A.; Xia, Y.; Zhao, D. Sol–Gel Design Strategy for Ultradispersed TiO_2 Nanoparticles on Graphene for High-Performance Lithium Ion Batteries. *J. Am. Chem. Soc.* **2013**, *135*, 18300–18303.

31. Zhang, F.; Cao, H.; Yue, D.; Zhang, J.; Qu, M. Enhanced Anode Performances of Polyaniline– TiO_2 –Reduced Graphene Oxide Nanocomposites for Lithium Ion Batteries. *Inorg. Chem.* **2012**, *51*, 9544–9551.

32. Qiu, J.; Zhang, P.; Ling, M.; Li, S.; Liu, P.; Zhao, H.; Zhang, S. Photocatalytic Synthesis of TiO_2 and Reduced Graphene Oxide Nanocomposite for Lithium Ion Battery. *ACS Appl. Mater. Interfaces* **2012**, *4*, 3636–3642.

33. Wang, D.; Choi, D.; Li, J.; Yang, Z.; Nie, Z.; Kou, R.; Hu, D.; Wang, C.; Saraf, L. V.; Zhang, J.; et al. Self-Assembled TiO_2 –Graphene Hybrid Nanostructures for Enhanced Li-Ion Insertion. *ACS Nano* **2009**, *3*, 907–914.

34. Zhang, H.; Lv, X. J.; Li, Y. M.; Wang, Y.; Li, J. H. P25–Graphene Composite as a High Performance Photocatalyst. *ACS Nano* **2010**, *4*, 380–386.

35. Williams, G.; Seger, B.; Kamat, P. V. TiO_2 –Graphene Nanocomposites. UV-Assisted Photocatalytic Reduction of Graphene Oxide. *ACS Nano* **2008**, *2*, 1487–1491.

36. Du, J.; Lai, X.; Yang, N.; Zhai, J.; Kisailus, D.; Su, F.; Wang, D.; Jiang, L. Hierarchically Ordered Macro Mesoporous TiO_2 Graphene Composite Films: Improved Mass Transfer, Reduced Charge Recombination, and Their Enhanced Photocatalytic Activities. *ACS Nano* **2011**, *5*, 590–596.

37. Li, B.; Zhang, X.; Li, X.; Wang, L.; Han, R.; Liu, B.; Zheng, W.; Li, X.; Liu, Y. Photo-Assisted Preparation and Patterning of Large-Area Reduced Graphene Oxide– TiO_2 Conductive Thin Film. *Chem. Commun.* **2010**, *46*, 3499–3501.

38. Chen, C.; Cai, W.; Long, M.; Zhou, B.; Wu, Y.; Wu, D.; Feng, Y. Synthesis of Visible-Light Responsive Graphene Oxide/ TiO_2 Composites with p/n Heterojunction. *ACS Nano* **2010**, *4*, 6425–6432.

39. Xiang, Q.; Yu, J.; Jaroniec, M. Enhanced Photocatalytic H_2 -Production Activity of Graphene-Modified Titania Nanosheets. *Nanoscale* **2011**, *3*, 3670–3678.

40. Marcano, D. C.; Kosynkin, D. V.; Berlin, J. M.; Sinitskii, A.; Sun, Z.; Slesarev, A.; Alemany, L. B.; Lu, W.; Tour, J. M. Improved Synthesis of Graphene Oxide. *ACS Nano* **2010**, *4*, 4806–4814.

41. Kobayashi, M.; Petrykin, V. V.; Kakihana, M.; Tomita, K.; Yoshimura, M. One-Step Synthesis of $\text{TiO}_2\text{(B)}$ Nanoparticles from a Water-Soluble Titanium Complex. *Chem. Mater.* **2007**, *19*, 5373–5376.

42. Marchand, R.; Brohan, L.; Tournoux, M. $\text{TiO}_2\text{(B)}$ a New Form of Titanium Dioxide and the Potassium Octatitanate $\text{K}_2\text{Ti}_8\text{O}_{17}$. *Mater. Res. Bull.* **1980**, *15*, 1129–1133.

43. Beuvier, T.; Plouet, M. R.; Brohan, L. Accurate Methods for Quantifying the Relative Ratio of Anatase and $\text{TiO}_2\text{(B)}$ Nanoparticles. *J. Phys. Chem. C* **2009**, *113*, 13703–13706.

44. Xiang, Q. J.; Yu, J. G.; Jaroniec, M. Preparation and Enhanced Visible-Light Photocatalytic H_2 -Production Activity of Graphene/ C_3N_4 Composites. *J. Phys. Chem. C* **2011**, *115*, 7355–7363.

45. Rao, C. N. R.; Sood, A. K.; Subrahmanyam, K. S.; Govindaraj, A. Graphene: The New Two-Dimensional Nanomaterial. *Angew. Chem., Int. Ed.* **2009**, *48*, 7752–7777.

46. Stankovich, S.; Dikin, D. A.; Piner, R. D.; Kohlhaas, K. A.; Kleinhammes, A.; Jia, Y.; Wu, Y.; Nguyen, S. T.; Ruoff, R. S. Synthesis of Graphene-Based Nanosheets via Chemical Reduction of Exfoliated Graphite Oxide. *Carbon* **2007**, *45*, 1558–1565.

47. Sun, L.; Zhao, Z.; Zhou, Y.; Liu, L. Anatase TiO_2 Nanocrystals with Exposed $\{001\}$ Facets on Graphene Sheets via Molecular Grafting for Enhanced Photocatalytic Activity. *Nanoscale* **2012**, *4*, 613–620.

48. Ferrari, A. C. Raman Spectroscopy of Graphene and Graphite: Disorder, Electron–Phonon Coupling, Doping and Nonadiabatic Effects. *Solid State Commun.* **2007**, *143*, 47–57.

49. Panduwinata, D.; Gale, J. D. A First Principles Investigation of Lithium Intercalation in $\text{TiO}_2\text{-B}$. *J. Mater. Chem.* **2009**, *19*, 3931–3940.

50. Breault, T. M.; Bartlett, B. M. Lowering the Band Gap of Anatase-Structured TiO_2 by Coalloying with Nb and N: Electronic Structure and Photocatalytic Degradation of Methylene Blue Dye. *J. Phys. Chem. C* **2012**, *116*, 5986–5994.

51. Grabstanowicz, L. R.; Gao, S.; Li, T.; Rickard, R. M.; Rajh, T.; Liu, D.-J.; Xu, T. Facile Oxidative Conversion of TiH_2 to High-Concentration Ti^{3+} -Self-Doped Rutile TiO_2 with Visible-Light Photoactivity. *Inorg. Chem.* **2013**, *52*, 3884–3890.

52. Akhavan, O.; Ghaderi, E. Photocatalytic Reduction of Graphene Oxide Nanosheets on TiO_2 Thin Film for Photo-inactivation of Bacteria in Solar Light Irradiation. *J. Phys. Chem. C* **2009**, *113*, 20214–20220.

53. Park, J. H.; Kim, S.; Bard, A. J. Novel Carbon-Doped TiO_2 Nanotube Arrays with High Aspect Ratios for Efficient Solar Water Splitting. *Nano Lett.* **2006**, *6*, 24–28.

54. Wang, Y.; Li, H.; Ji, L.; Liu, X.; Wu, Y.; Lv, Y.; Fu, Y.; Zhou, H.; Chen, J. Synthesis and Characterization of Titanium-Containing Graphite-Like Carbon Films with Low Internal Stress and Superior Tribological Properties. *J. Phys. D: Appl. Phys.* **2012**, *45*, 295301–295310.

55. Dong, F.; Guo, S.; Wang, H.; Li, X.; Wu, Z. Enhancement of the Visible Light Photocatalytic Activity of C-Doped TiO_2 Nanomaterials Prepared by a Green Synthetic Approach. *J. Phys. Chem. C* **2011**, *115*, 13285–13292.

56. Shah, M. S. A. S.; Park, A. R.; Zhang, K.; Park, J. H.; Yoo, P. J. Green Synthesis of Biphasic TiO_2 -Reduced Graphene Oxide Nanocomposites with Highly Enhanced Photocatalytic Activity. *ACS Appl. Mater. Interfaces* **2012**, *4*, 3893–3901.
57. Becerril, H. A.; Mao, J.; Liu, Z.; Stoltenberg, R. M.; Bao, Z.; Chen, Y. Evaluation of Solution-Processed Reduced Graphene Oxide Films as Transparent Conductors. *ACS Nano* **2008**, *2*, 463–470.
58. Zhu, C. Z.; Guo, S. J.; Wang, P.; Xing, L.; Fang, Y. X.; Zhai, Y. M.; Dong, S. J. One-Pot, Water-Phase Approach to High-Quality Graphene/ TiO_2 Composite Nanosheets. *Chem. Commun.* **2010**, *46*, 7148–7150.
59. Etacheri, V.; Michlits, G.; Seery, M. K.; Hinder, S. J.; Pillai, S. C. A Highly Efficient $\text{TiO}_{2-x}\text{C}_x$ Nano-Heterojunction Photocatalyst for Visible Light Induced Antibacterial Applications. *ACS Appl. Mater. Interfaces* **2013**, *5*, 1663–1672.
60. Etacheri, V.; Seery, M. K.; Hinder, S. J.; Pillai, S. C. Nanostructured $\text{Ti}_{1-x}\text{S}_x\text{O}_{2-y}\text{N}_y$ Heterojunctions for Efficient Visible-Light-Induced Photocatalysis. *Inorg. Chem.* **2012**, *51*, 7164–7173.
61. Armstrong, A. R.; Armstrong, G.; Canales, J.; García, R.; Bruce, P. G. Lithium-Ion Intercalation into TiO_2 -B Nanowires. *Adv. Mater.* **2005**, *17*, 862–865.
62. Bueno, P. R.; Leite, E. R. Nanostructured Li Ion Insertion Electrodes. 1. Discussion on Fast Transport and Short Path for Ion Diffusion. *J. Phys. Chem. B* **2003**, *107*, 8868–8877.